Template-free synthesis of carbon-doped boron nitride nanosheets for enhanced photocatalytic hydrogen evolution

Liuyong Chen[a], Min Zhou[a], Zhishan Luo[a], Muhammad Wakeel[b], Abdullah M. Asiri[c], Xinchen Wang[a,*]

[a] State Key Laboratory of Photocatalysis on Energy and Environment, College of Chemistry, Fuzhou University, Fuzhou 350002, PR China
[b] Department of Environmental Science, Bahauddin Zakariya University, Multan, Pakistan
[c] Chemistry Department, Faculty of Science, King Abdulaziz University, Jeddah 21589, Saudi Arabia

ARTICLE INFO

ABSTRACT

Photocatalytic hydrogen production from water is a promising strategy for the direct conversion of sunlight into chemical energy, which is considered as a long-term and sustainable solution to address worldwide energy and environmental issues. Herein, we develop carbon doped boron nitride (BCN) as metal-free photocatalysts by using solid-gas reaction and molecular design method of boron source. Four kinds of boron carbon nitride (BCN) were synthesized through mixed glucoses with melamine phosphate borate (MPB), melamine borate (MB), boric acid (BA) and boron oxide (BO), respectively. It can be found that the morphology of BCN-MPB (nanosheets) is different from bulk BCN-MB, bulk BCN-BA and bulk BCN-BO. The BCN-MPB nanosheets show much higher specific surface area, the longer lifetime of photoexcited charge carriers, and the stronger electron transport ability compared to those of bulk BCN. Thus, BCN-MPB nanosheets exhibit significantly improved photocatalytic hydrogen activities under visible light illumination compared to those of bulk BCN. Our work represents a facile and template-free synthesis strategy for the rational design of eco-friendly, stable and inexpensive photo-catalysts, and paves new pathways for tuning their photoreactivity in sustainable light-to-energy conversion.

1. Introduction

Concentrated efforts have been employed to seeking a promising and alternative way to alleviate the current worldwide energy and environmental issues. Artificial photosynthesis, which imitates the natural conversion and generation of chemical fuels, is deemed as the promising strategy of overcoming the energy and environmental issues [1–5]. Particularly, photocatalytic hydrogen production has attracted tremendous interest as a clean, sustainable and economical technique for solar-to-hydrogen conversion [1,6–11]. Although great efforts have been devoted to developing semiconductor photocatalysts in the past forty years, it remains a great challenge to develop stable, efficient, and low-cost sunlight-driven photocatalysts for practical applications [12–14]. Recently, some metal-free photocatalysts has emerged, including elemental (red and black) phosphor [15–17], boron [18], and sulfur [19], the binary boron phosphide [20], boron carbide [21] and carbon nitride [22]. The development of the stable photocatalysts from earth-abundant and lightweight elements may be open up new opportunities for artificial photosynthesis.

Graphene, the two-dimensional (2D) monolayer of sp2-bonded carbon, has been put on the foreground of material science because of its fascinating physical and chemical properties [23–26]. Structurally similar to graphene, layered hexagonal boron nitride (h-BN) has received much attention due to its unique thermoelectric [27], optical [28], absorption [29], and mechanical [27,30] properties. Recently, the structural similarity between graphene and h-BN motivates researchers to achieve their hybrid, boron carbon nitrides (BCN) [31–33]. Ternary BCN features the capability of bandgap engineering, which is of great significance in many applications, including luminescenc [34,35], electronics [31], dehydrogenation of ethylbenzene [36], solar energy converters [37,38] etc. Due to these attractive features, theoretical works and experimental studies have recently revealed that the band-gap of nanostructured boron carbon nitride can be adjusted by manipulating the carbon content self-doped into the h-BN lattice, thus considerably modifying its light absorption and emission properties [31,37–39]. However, the theoretical and experimental investigation on the synthesis and photocatalytic performances of BCN materials is still in its infancy due to the difficulty to control the texture and the band structure [37,38].

Thus far, there have been a mass of reports on BCN synthesis

---

* Corresponding author.
  E-mail address: xcwang@fzu.edu.cn (X. Wang).

methods, including thermal chemical vapor deposition (CVD) [40], catalytic CVD technique [41], radio frequency magnetron sputtering [42] and plasma-enhanced CVD (PECVD) [43,44]. Nevertheless, these methods usually required high temperature conditions, expensive templates and sophisticated apparatus with the careful synthesis processes. Traditional B-containing gaseous precursors such as boron trichloride, diborane, methylamine borane and trimethylamine borane together with carbon chloride or acetylene or acetonitrile have been explored for BCN under ammonia as feedstock gases [40,45–49]. However, these B-containing compounds are hypertoxic and dangerous, which restricts their further applications. In addition, researchers also have developed some of the synthesis methods of BCN which is mainly rely on separate sources for carbon and BN [49,50]. However, the resultant products are often composed of small clusters of carbon and BN composites [51]. This limits their overall tuneability in terms of electrical and optical properties [45,51]. Thus, these issues have stimulated us to develop a facile method to produce BCN and explore its photoredox functions.

In this article, a ternary structure of BCN was generated by a facile and template-free method via mixed glucoses, urea with different boron source, and was applied to catalytic hydrogen evolution from water under visible light illumination. It can be found that BCN nanosheets can be only synthesized by using melamine phosphate borate as boron source, and we failed to detect phosphorus signal in X-Ray photoelectron spectroscopy (XPS). During the reaction process, the decomposition of phosphate of melamine phosphate borate released gases and blew precursors into numerous large bubbles compared to other boron sources, yielding BCN-MPB nanosheets. The BCN-MPB nanosheets with thickness of about 4.2 nm possess enhanced specific surface area, improved electron transport ability and increased separation rate of electrons and holes, revealing the significant enhancement in photocatalytic hydrogen production under visible light compared to those of bulk BCN.

2. Experimental

2.1. Synthesis of the photocatalysts

Synthesis of BCN-MPB nanosheets: Melamine phosphate borate (MPB) was fabricated from melamine ($C_3H_6N_6$, 99%), boric acid (H_3BO_3, 99.9%) and phosphoric acid (H_3PO_4, 85%) via a stepwise method. First, 17.02 g phosphoric acid was added into 50 ml deionized water at 50 °C under stirring and the mixture was stirred at 50 °C for 10 min, 18.60 g melamine was added into the above phosphoric acid solution slowly and the mixture was stirred at 50 °C for 2 h. The solution was cooled down, filtrated, washed with water several times and then dried at 80 °C overnight to obtain melamine phosphate (MP) adducts. Second, 6.70 g boric acid was dissolved in deionized water (45 ml) at 80 °C under stirring for 10 min, and 16.20 g MP was added into the above boric acid solution slowly and the mixture was stirred at 80 °C for 3 h. When the solution was cooled down, and followed by filtration, washed with water several times and dried at 70 °C overnight, thus producing 16.58 g of MPB adducts. Typically, 2 g glucose (99%), 1 g MPB and 2 g urea (99%) were grinded fully with an agate mortar. After that, mixture was put into a horizontal tube furnace and was then heated in an ammonia atmosphere at 1050 °C for 5 h with a ramp rate of 5 °C min^{-1}. The obtained sample was washed with 0.1 M HCl and was named as BCN-MPB. (Some information of MPB were added to the Supporting Information).

Synthesis of bulk BCN-MB: Melamine borate (MB) were obtained from melamine and boric acid as described previously [52]. Briefly, melamine (15 mmol) was dissolved in deionized water (50 ml) at 90 °C, and boric acid (30 mmol) was dissolved and stirred in deionized water (20 ml) at 90 °C under stirring. Then boric acid solution was added into the above melamine solution slowly and the mixture was stirred at 90 °C for 30 min. The solution was cooled down, followed by filtration

and dried at 70 °C overnight. Glucose (2 g), melamine borate (1 g) and urea (2 g) were grinded fully with an agate mortar. After that, mixture was put into a horizontal tube furnace and was then heated at 1050 °C for 5 h in an ammonia atmosphere with the flow rate of 200 cm^3 min^{-1}. The obtained sample was washed with 0.1 M HCl and was denoted as BCN-MB.

Synthesis of bulk BCN-BA: Typically, glucose (2 g), boric acid (1 g) and urea (2 g) were grinded fully with an agate mortar. After that, mixture was put into a horizontal tube furnace and was then heated at 1050 °C for 5 h in an ammonia atmosphere. The obtained sample was washed with 0.1 M HCl and was named as BCN-BA.

Synthesis of bulk BCN-BO: 2 g glucose, 1 g boron oxide (B_2O_3, 99.9%) and urea (2 g) were grinded fully with an agate mortar. After that, mixture was put into a horizontal tube furnace and was then heated at 1050 °C for 5 h in an ammonia atmosphere. The obtained sample was washed with 0.1 M HCl and was denoted as BCN-BO.

2.2. Characterization

Powder X-ray diffraction (XRD) measurements were carried out on a Bruker D8 Advance X-ray diffractometer with Cu-Kα1 radiation. Fourier transform infrared (FTIR) spectra were operated on a thermo Nicolet Nexus 670 FTIR spectrometer with KBr as the diluents. The UV-Vis diffuse reflectance spectra (DRS) were measured on a Varian Cary 500 Scan UV-Visible system with an integrating sphere using BaSO4 as a reference. Photoluminescence (PL) spectra were operated on an Edinburgh FI/FSTCSPC 920 spectrophotometer. X-Ray photoelectron spectroscopy (XPS) data were obtained on a Thermo Scientific ESCALAB250 instrument with a monochromatized Al Kα line source (200 W). All binding energies were referenced to the C 1s peak at 284.6 eV of surface adventitious carbon. Nitrogen adsorption-desorption isotherms were performed at 77 K using Micromeritics ASAP 3035 equipment. The pore size distribution was estimated with Brrett-Joyner-Halenda (BJH) and the specific surface area (SSA) was determined with the Beunauer-Emmett-Teller (BET) method. The scanning emission microscope (SEM) measurements were carried out by using Hitachi S4800 Field Emission Scanning Electron Microscope. Atomic force microscopy (AFM) image was obtained on a Nano Scope IVA instrument. Transmission electron microscopy (TEM) was obtained using Tecnai G2F20 microscopy. Thermogravimetric (TG) analysis was carried out in Ar using a TGA/DSC 3 (Mettler-Toledo, Switzerland) from 30 to 1050 °C with a heating rate of 10 °C min^{-1}. Electron paramagnetic resonance (EPR) measurements were operated on a Bruker model A300 spectrometer. Electrochemical measurements were conducted with a BAS Epsilon Electrochemical System in a conventional three electrode cell, using a Pt plate as the counter electrode and an saturated calomel electrode as the reference electrode, the working electrode was obtained by dip-coating catalyst slurry on FTO glass. FTO glass was cleaned by sonication for 0.5 h and dried at 80 °C. The 5 mg sample was dispersed in 0.8 ml DMF solution by sonication to get a slurry. The slurry were spread onto pretreated FTO glass and dried in the air.

2.3. Photocatalytic reaction

Photocatalytic hydrogen production was operated in a Pyrex top-irradiation reactor linked to a glass closed gas-circulation system. Hydrogen production was performed by dispersing catalyst powder (50 mg) in an aqueous solution (100 mL) containing triethanolamine (10 vol. %, as the sacrificial electron donor). 1 wt. % Pt was loaded on the surface of photocatalyst by the in-situ photodeposition approach. The reactant solution was evacuated several times to remove air completely before irradiation under a 300 W Xe-lamp with a working current of 15 A. The wavelength of the incident light was operated by applying some appropriate long-pass cut-off filters. The temperature of the reaction solution was maintained at 12 °C by a flow of cooling
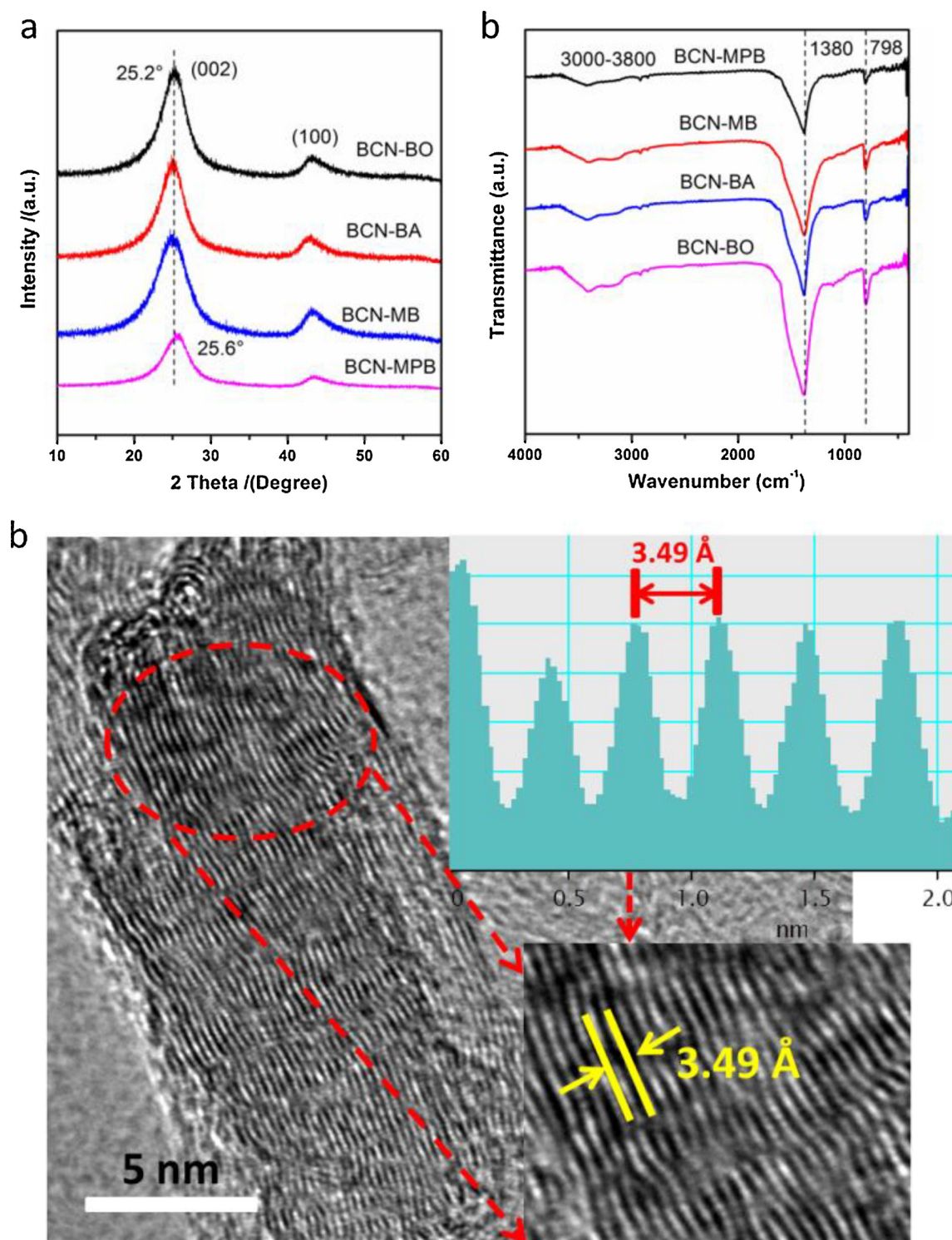
Fig. 1. (a) XRD patterrns of BCN-MPB, BCN-MB, BCN-BA, and BCN-BO. (b) HRTEM images of the BCN-MPB sample. (c) FTIR spectra of BCN-BO, BCN-BA, BCN-MB, and BCN-MPB.

water. The generated gases were analyzed by gas chromatography equipped with a thermal conductive detector (TCD), and a 5 Å molecular sieve column, using Argon as the carrier gas.

3. Results and discussion

X-ray diffraction patterns (XRD), Fourier transform infrared (FT-IR) spectroscopy and X-ray photoelectron spectroscopy (XPS) analysis were carried out to analyze the formation of the prepared BCN catalysts.

Fig. 1a shows the XRD patterns of the produced samples with different boron sources. It could be observed that all samples have two similar XRD characteristic diffraction peaks at around 25.4 and 42.7°, attributed to the (002) and (100) crystal planes of the graphitic-like crystal structure of h-BN [38,52–54], respectively. Furthermore, the low-angle reflection peak of BCN-MPB nanosheets is slightly up-shifted to 25.6° with respect to other bulk BCN (25.2°), suggesting a reduced interlayer distance between the basic sheets [55,56]. In addition, XRD patterns reveal a deduced lattice parameter (d_{002} = 3.48 Å) of BCN-MPB, which
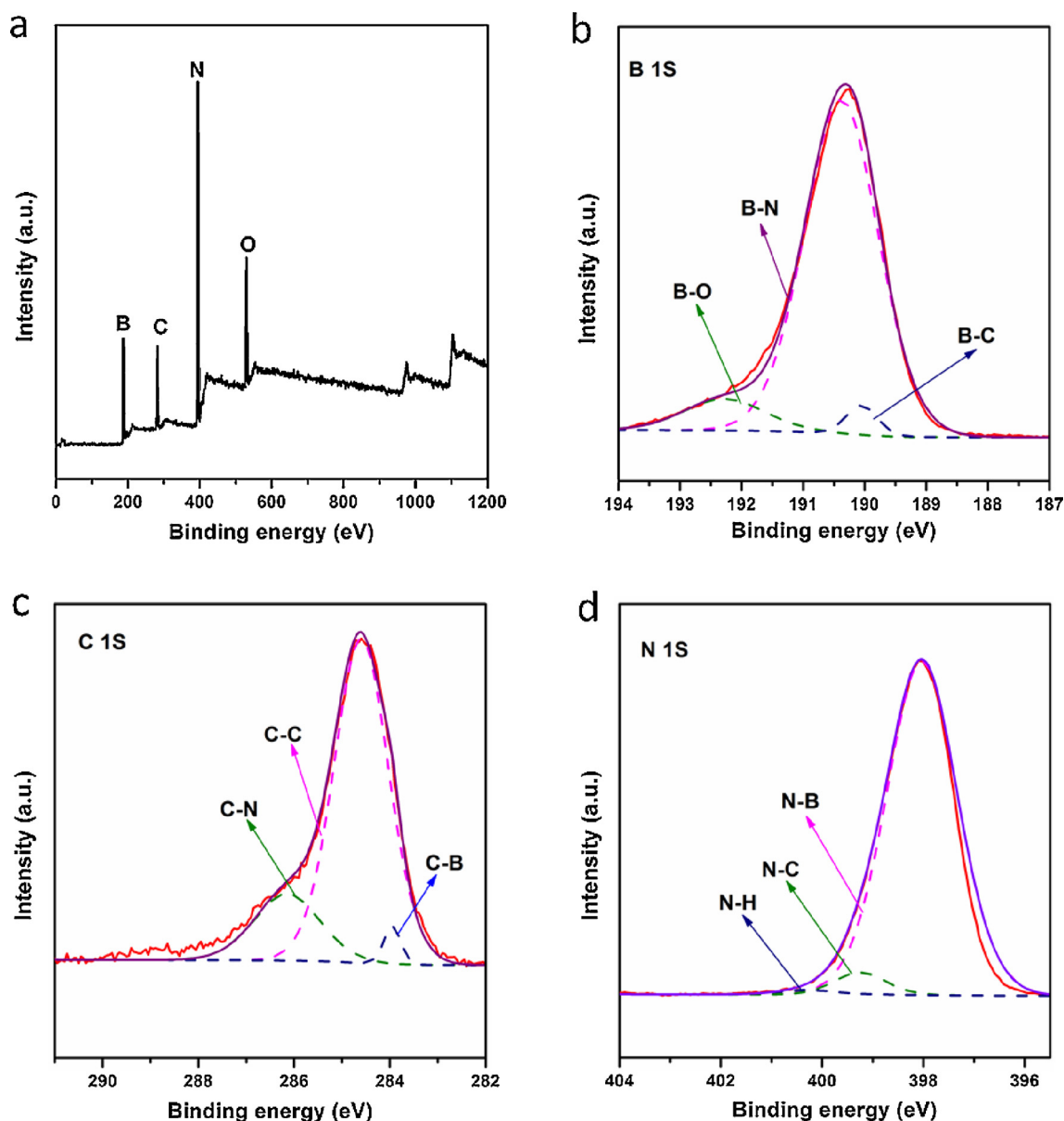
**Fig. 2.** XPS survey and hight-resolved spectra of the BCN-MPB sample.

is corresponding to (002) peak. The interplanar distance are further conformed by high-resolution transmission electron microscopy (HRTEM), which shows the (002) distance of BCN-MPB nanosheets is about 3.49 Å (inset in Fig. 1b). This d002 value is in accordance with the deduced value of XRD. FT-IR spectroscopy confirms the disordered graphitic structure of BCN samples (Fig. 1c) with bands at 1380 and 798 cm^{-1}, which correspond to characteristic of sp^2-bonded B–N in-plane transverse stretching vibrations and out-of-plane B–N–B bending vibrations, respectively [37,38,57]. Broad bands in the 3000-3800 cm^{-1} region for all samples are observed, which is ascribed to physisorbed H$_2$O [37,58]. In addition, we failed to detect the vibrations of C–N bonds since it is overlapped by that of B–N bands around 1100–1300 cm^{-1}. But in the high-resolution C 1s XPS spectrum (Fig. 2c), we could observe the existence of C-related bonds.

As shown in the survey XPS spectrum (Fig. 2a), only four elements of B, C, N and O are detected. The O 1s peak is possibly due to un-reacted B–O and the surface absorbed H$_2$O. The former may be attributed to surface impurities in the BCN-MPB nanosheets [31,38] and the latter is confirmed by the FT-IR result (Fig. 1c). The functional groups and bonding characteristic of BCN-MPB are further determined by the

high resolution B 1s, C 1s and N 1s spectra (Fig. 2b–d). There are three peaks occuring at 189.9, 190.3 and 192.4 eV in the B 1s spectrum (Fig. 2b), corresponding to B–C, B–N, and B–O bands, respectively [59]. The presence of B–O band can be ascribed to the defective sites or surface impurities in the BCN-MPB nanosheets [45]. As shown in Fig. 2c, the C 1s spectrum of BCN-MPB sample can be deconvoluted into three peaks situated at 283.6, 284.6 and 285.7 eV, which are assigned to C–B, C=C and C–N bands, respectively [37,59]. The deconvoluted N 1s spectrum (Fig. 2d) distinguishes three peaks located at 397.9, 398.9 and 400.6 eV, respectively. The main component centered at 397.9 eV corresponds to N-B bonding, and the subpeaks at 398.9 and 400.6 eV are assigned to N–C bands and N–H bands, respectively [37,59]. Thus, XPS analysis proved that carbon has been incorporated in the h-BN lattice [38].

The nanosheet structure of the BCN-MPB is readily identified with scanning electron microscopy (SEM), transmission electron microscopy (TEM) and Atomic force microscopy (AFM). Flake-like morphology can be observed in SEM images of the BCN-MPB (Fig. 3a and Fig. S1a, b), which is similar to graphene or graphene oxide. As shown in Fig. 3b–d, the large-bulk morphologies of BCN-MB, BCN-BA and BCN-BO can be
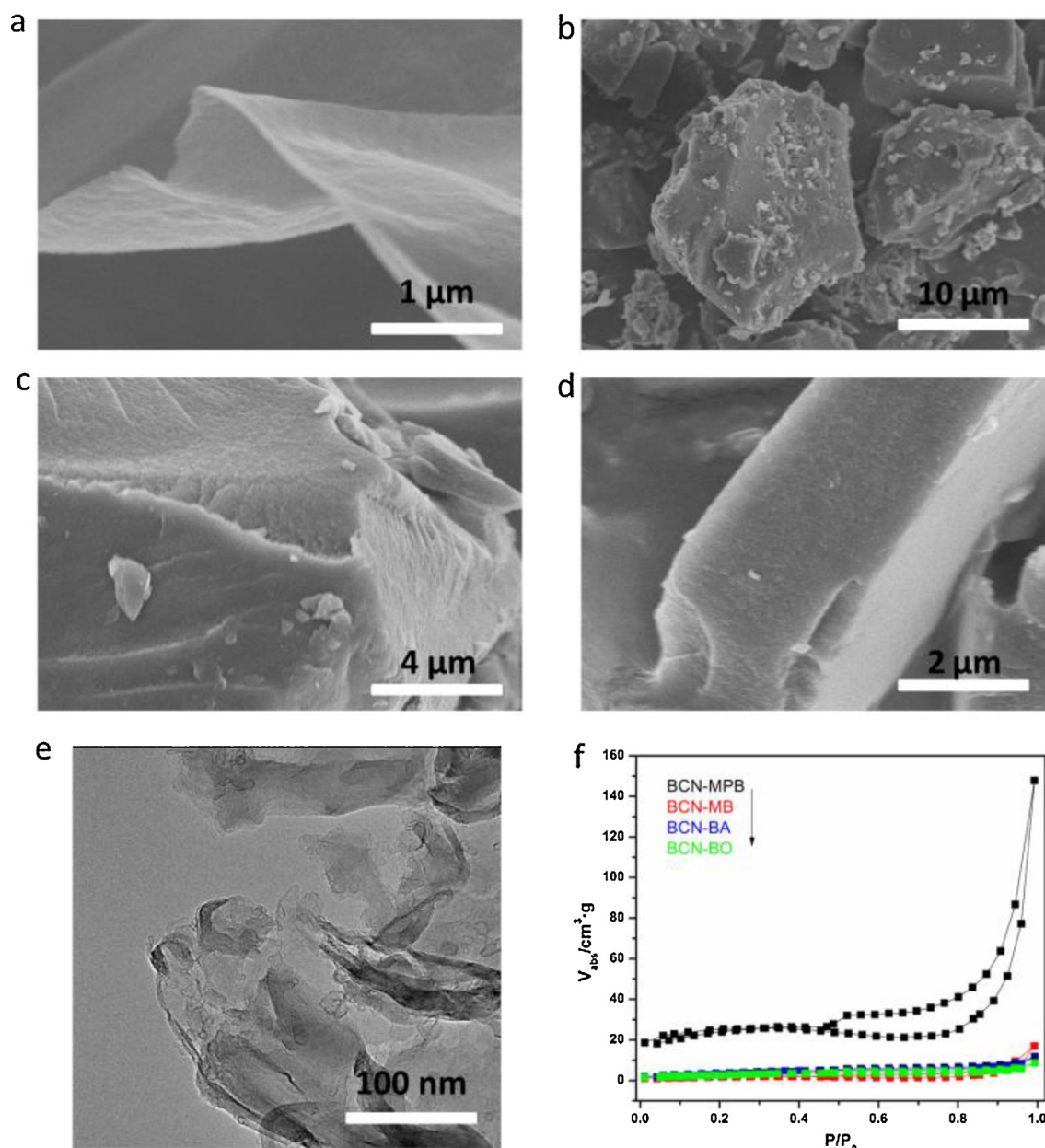
Fig. 3. SEM images of: (a) BCN-MPB. (b) BCN-MB. (c) BCN-BA. and (d) BCN-BO. (e) TEM image of the BCN-MPB sample. (f) N2 adsorption and desorption isotherms of BCN-MPB, BCN-MB, BCN-BO, and BCN-BA.

clearly observed. During the reaction process, the decomposition of melamine phosphate borate released gases and blows the precursor into numerous large bubbles compared to other boron sources, yielding BCN-MPB nanosheets. To obtain more information about the morphology and micro-structure of the samples, TEM analysis was implemented. As shown in Fig. 3e, image of BCN-MPB materials appears layered platelet-like surface morphology. In addition, the basic sheet edge tends to bend, which may lead to the minimized surface energy of the sheet. The thickness of BCN-MPB nanosheets are further measured with AFM technology. Their AFM images and thickness analyses (Fig. 4a, b and inset in Fig. 4a, b) show an average thickness of approximately 4.2 nm. The homogeneity of ternary BCN alloys was proved by elemental mapping analysis, which shows uniform distribution of boron, carbon and nitrogen elements in the BCN-MPB nanosheets throughout the whole selected area (Fig. 4c).

The nitrogen adsorption − desorption isotherms of BCN-MPB, BCN-MB, BCN-BO, and BCN-BA were displayed in Fig. 3f, BCN-MPB nanosheets exhibits the largest surface area among all samples, suggesting that it possesses more catalytically active sites than those of bulk BCN [60]. The specific surface areas and hydrogen (H_2) evolution rate of BCN samples were summarized in Table S1, indicating that the higher specific surface area (BCN-MPB) results in an increased surface reactivity for the photocatalytic reaction under visible light compared to those of bulk BCN.

Thermogravimetric (TG) analysis was carried out in Ar to further study the mechanism of the formation of BCN-MPB nanosheets (Fig. 5). Boric acid (BA) presented a weight loss of about 43.2% in the temperature ranging from 110 to 520 ℃, corresponding to the decomposition of BA to produce thermal-stable B_2O_3. A weight loss of about 73.1% was recorded for Melamine borate (MB) from approximately 120 to 1000 ℃, which are assigned to the decomposition of MB to produce thermal-stable B_2O_3. The weight loss for Melamine phosphate borate (MPB) was about 77% from approximately 150 to 1000 ℃, which was ascribed to the decomposition of MPB to produce thermal-stable B_2O_3.
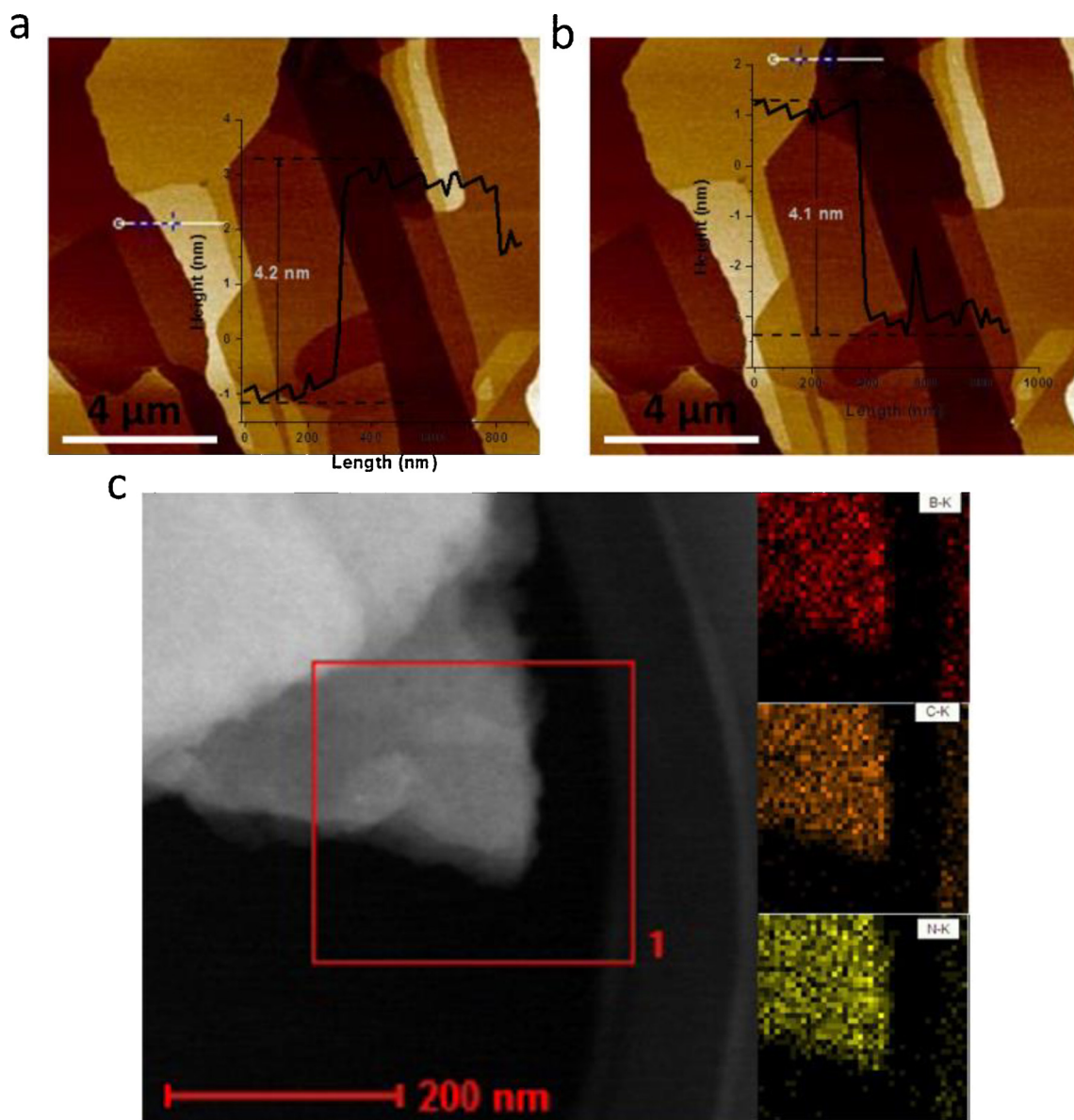
Fig. 4. AFM images of (a, b) BCN-MPB. The insets in the AFM images show the corresponding cross-sectional profile. (c) Typical TEM image of BCN-MPB and elemental mapping images of B, C, and N.

In TG curve, it can be clearly observed that the weight loss for MPB is more than MB and BA. Thus, during the reaction process, the decomposition of melamine phosphate borate released gases and blows the precursor into numerous large bubbles compared to other boron sources, yielding BCN-MPB nanosheets.

In order to study the electronic band structures of the nanosheets and bulk materials, the optical absorption spectrum and the Mott-Schottky plots were measured. With reduced dimensionality of BCN materials, excitonic effect become more prominent as a consequence of the quantum confinement effect (QCE) [61]. In low dimensional systems, enhanced electron-electron correlation leads to the enlargement of electronic band gaps. However, the confinement-induced large overlap between the electron and hole wave functions gives rise to reduced screening between the light-excited electron and hole, and thus results in the formation of strongly-bound neutral excitons via Coulomb interactions [61].The optical absorption of the as-produced BCN-MPB nanosheets and bulk BCN samples were obtained by using the diffuse reflectance spectrum (Fig. 6a). It can be clearly observed that the intrinsic absorption edge of BCN-MPB nanosheets obviously blue-shift compared to bulk BCN. As shown in Fig. 6b, the bandgaps energy of BCN-MPB nanosheets was estimated to be 1.99 eV from the $(Ahv)^2$ versus photon-energy plotst, which is greater than those of bulk BCN samples. The bandgap of BCN can be adjusted by tuning carbon content doped into the h-BN lattice. The bandgap of BCN gradually decreased with increasing amounts of carbon [37,38]. However, in the elemental analysis by XPS (Table S2), it can be found that the carbon content of BCN-MPB nanosheets is much higher than those of bulk BCN samples. This result elucidates that the larger bandgap is mainly attributed to the QCE by shifting the conduction and valence band edges in opposite directions rather than the change of carbon content incorporated in the h-BN lattice [62]. Apparently, the Mott-Schottky plots of BCN-MPB nanosheets and bulk BCN samples under 1.8KHZ disclose the typical n-type property of semiconductors due to the positive slope of the linear plots (Fig. 6c) [63,64]. More importantly, the flat band potentials of BCN-MPB nanosheets, bulk BCN-BA, bulk BCN-BO and bulk BCN-MB are around -0.93, -0.83, -0.66 and -0.59 V, respectively, using saturated calomel electrode as reference. The large shift in the conduction bands (CB) of BCN-MPB nanosheets is useful for enhancing the photocatalytic hydrogen evolution activity owing to the larger rmodynamic driving force of the hydrogen proton compared to those of bulk BCN samples

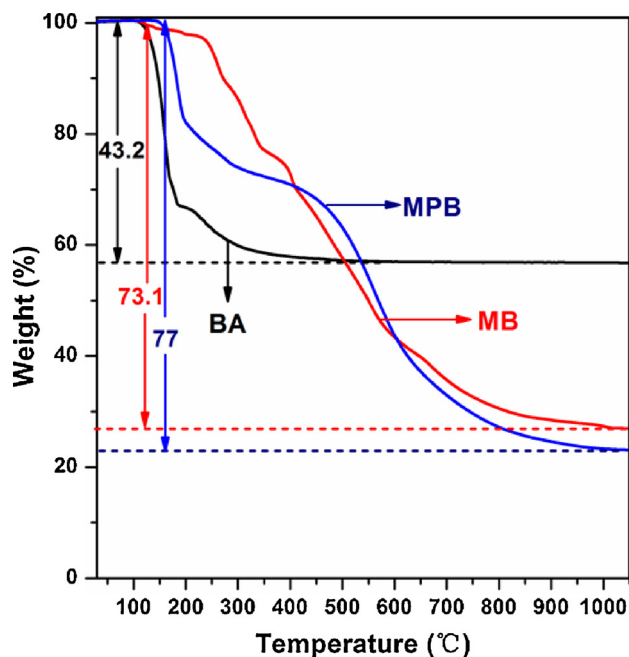**Fig. 5.** TG analyses of sample BA, MB, and MPB.

[63,65–67]. In addition, the band positions of BCN-MPB nanosheets and bulk BCN samples were estimated to straddle the redox potential of water (Fig. S2), and the conduction and valence band edges of BCN-MPB nanosheets shift in opposite directions compared to bulk BCN samples.

Next, room-temperature electron paramagnetic resonance (EPR) analysis was carried out to investigate the spatial redistribution of charge carriers of as-prepared materials (Fig. 7a). The EPR intensity of BCN-MPB nanosheets is the strongest among the four samples, which suggests that the density state of conduction band electrons were increased after the donation of electron from carbon atoms [37,68]. In addition, the EPR spectra of BCN samples show the similar single Lorentzian line centered at a g value of 2.0034 in the magnetic field from 3480 to 3550, which is attributed to lone pair electrons on carbon atoms in aromatic systems [69,70]. Furthermore, the electrochemical impedance spectra (EIS) and photocurrent spectroscopy were tested to investigate the electronic interaction in BCN-MPB nanosheets and bulk BCN-MB sample. As shown in Fig. 7b, the obviously increased photocurrent density is observed for BCN-MPB nanosheets compared to bulk BCN-MB, demonstrating the more efficient separation of photoinduced electrons and holes in BCN-MPB nanosheets. The EIS in Fig. 7c displays that BCN-MPB nanosheets exhibits much smaller diameter of the semicircular Nyquist plots compared to that of bulk BCN-MB, revealing that the decreased electron-transfer resistance in BCN-MPB nanosheets can effectively promote the interface charge transport compared to bulk
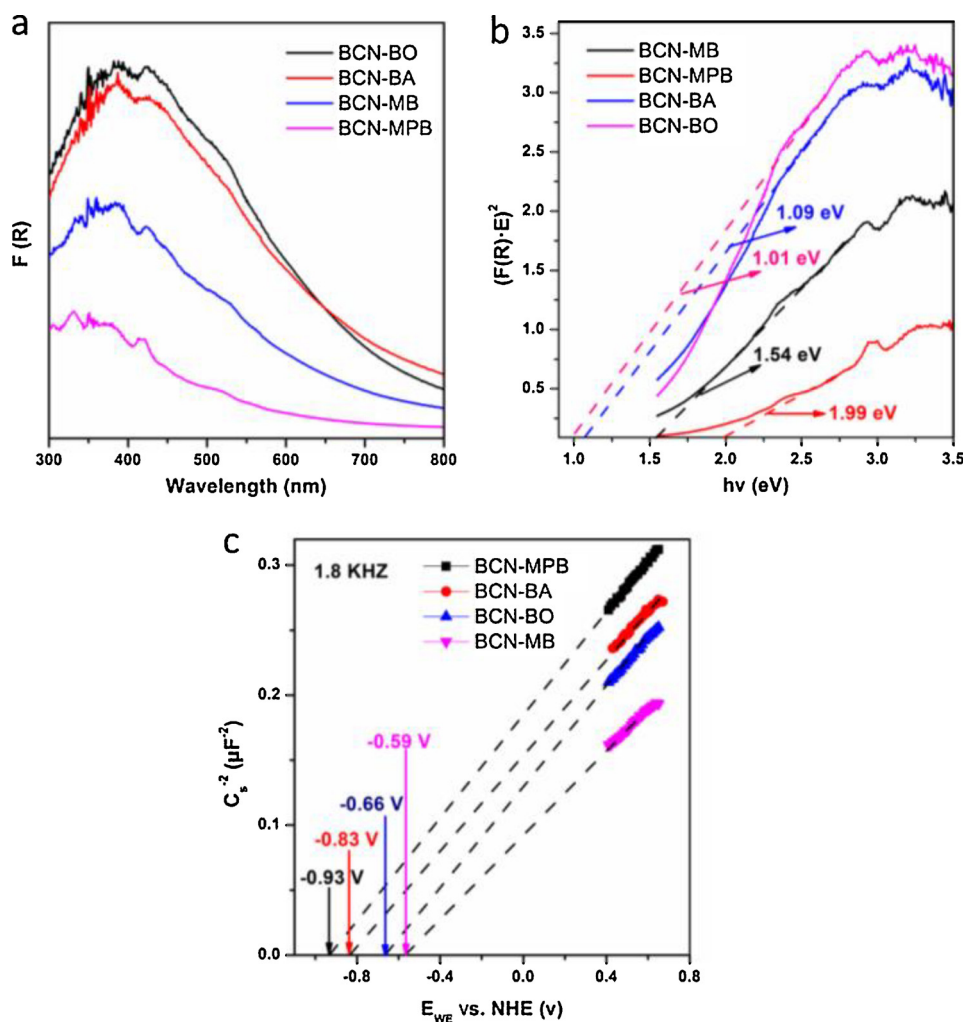

Fig. 6. (a) Uv-visible absorption spectra of BCN-MPB, BCN-MB, BCN-BA, and BCN-BO. (b) The Tauc plots of BCN-MPB, BCN-MB, BCN-BA, and BCN-BO vs photon energy. (c) The determination of the conduction band minimun of BCN-MPB, BCN-MB, BCN-BA, and BCN-BO by Mott-Schottky method in 0.2 M Na₂SO₄ aqueous aolution at 1.8 KHZ in the dark.
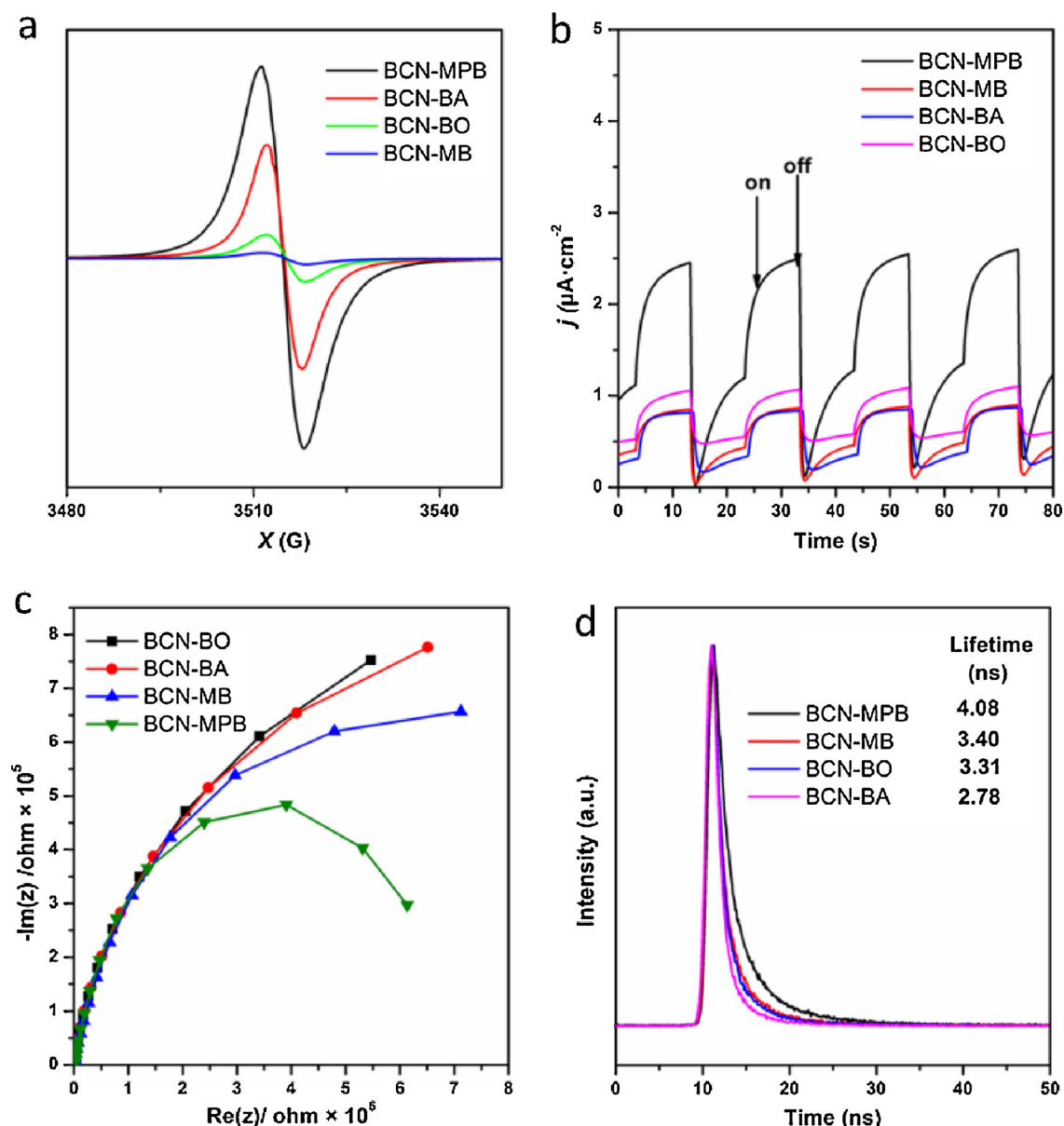
Fig. 7. (a) Room temperature EPR spectra of the as-prepared samples. (b) Photocurrent-time dependence of BCN-MPB, BCN-MB, BCN-BA, and BCN-BO. (c) EIS of the as-prepared samples. d) Time-resolved PL spectra of the as–prepared samples.

BCN-MB [63]. Besides, BCN-MPB nanosheets have longer photoluminescence (PL) lifetime (Fig. 7d, Table S3) compared to those of bulk BCN, which may be attributed to the changing electronic band structure derived from the QCE in the nanosheets and electron transport improvement [56,62].

The photocatalytic H_2 generation activity of all the catalysts were assessed in aqueous solutions containing triethanolamine as sacrificial reagents under a 300 W Xe-lamp with 420 nm cut-off filter. 1 wt. % Pt was loaded on the surface of photocatalyst by the in-situ photodeposition approach. The evolution of hydrogen was detected under visible light irradiation, but failed to be found in dark. As shown in Fig. 8a, BCN-MPB nanosheets has exhibited significantly improved photocatalytic performance with evidently higher hydrogen evolution rate (HER) compared to those of bulk BCN. The average HER of the BCN-MPB nanosheets is almost 5 times higher than bulk BCN-MB sample (see the Supporting Information, Fig. S3). Meanwhile, the trend of wavelength-dependent hydrogen evolution rate (WDHER) matches well with the optical absorption of BCN-MPB (Fig. 8b), elucidating that the H_2 evolution reaction is driven by the excitation of the BCN-MPB

photocatalyst [64].

The catalytic stability of BCN-MPB sample was assessed by performing the reaction for four cycles. In Fig. 8c, there was no obvious deactivation when catalysts were illuminated under continuous visible light irradition for 20 h. After 20 h of experiment, the structure of BCN-MPB nanosheets remians almost unchanged, as reflected by the FT-IR spectra and XRD patterns of the used photocatalyst (see the Supporting Information, Fig. S4). The enhancement in photocatalytic hydrogen production activity of BCN-MPB nanosheets is attributed to the synergistic effects of two-dimensional (2D) structural configuration with thickness of approximately 4.2 nm, large specific surface area, efficiently shortened length of charge migration, improved electron transport ability, as well as efficient separation of photo-generated charge carriers. All the experimental results proven that BCN-MPB nanosheets are successfully synthesized with higher HER compared to those of bulk BCN.
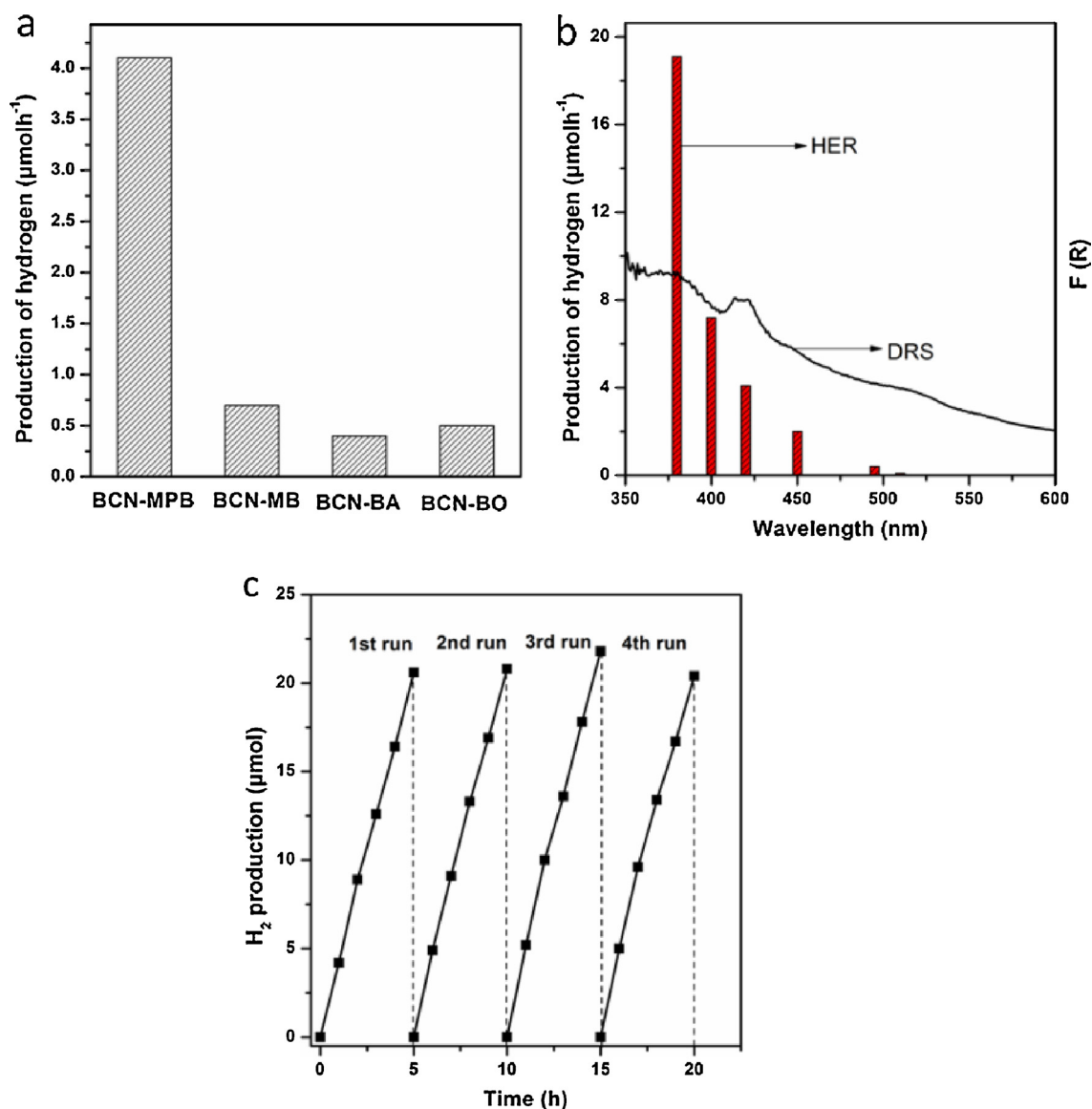
Fig. 8. (a) Hydrogen evolution rates (HER) of the as-prepared samples under visible light irradiation ($\lambda > 420$ nm). (b) Wavelength-dependent of HER by BCN-MPB under visible light irradiation. (c) Stability test of photocatalytic hydrogen evolution by BCN-MPB nanosheets under visible light irradiation ($\lambda > 420$ nm).

4. Conclusions

In summary, we have shown the synthesis of 2D BCN nanosheets by using solid-gas reaction and molecular design method of boron source. Due to its high specific surface area, improved electron transport ability, as well as efficient charge separation and transfer, BCN-MPB nanosheets exhibits superior phtocatalytic activity, which is almost 5 times higher than those of bulk BCN for hydrogen production under visible light. Our work also represents a facile synthesis strategy for the design of eco-friendly, stable, efficient and inexpensive photocatalysts. Benefiting from its 2D electron system, tunable bulk and surface properties, the potential applications of BCN nanosheets can be extended to various fields, such as sensors, photoelectrical devices, solar cells and energy storage devices.

Acknowledgments

Appendix A. Supplementary data

Supplementary material related to this article can be found, in the online version, at doi: https://doi.org/10.1016/j.apcatb.2018.09.034.

References

[1] A. Kudo, Y. Miseki, Chem. Soc. Rev. 38 (2009) 253–278.
[2] F.E. Osterloh, Chem. Soc. Rev. 42 (2013) 2294–2320.
[3] H. Tong, S. Ouyang, Y. Bi, N. Umezawa, M. Oshikiri, J. Ye, Adv. Mater. 24 (2012) 229–251.
[4] W. Wang, J. Chen, C. Li, W. Tian, Nat. Commun. 5 (2014) 4647–4657.
[5] L.-Z. Wu, B. Chen, Z.-J. Li, C.-H. Tung, Acc. Chem. Res. 47 (2014) 2177–2185.
[6] X. Chen, S. Shen, L. Guo, S.S. Mao, Chem. Rev. 110 (2010) 6503–6570.
[7] A. Kubacka, M. Fernández-García, G. Colón, Chem. Rev. 112 (2012) 1555–1614.
[8] C. Li, Y. Xu, W. Tu, G. Chen, R. Xu, Green Chem. 19 (2017) 882–899.
[9] C. Li, S. Yu, H. Dong, Y. Wang, H. Wu, X. Zhang, G. Chen, C. Liu, J. Colloid Interface Sci. 531 (2018) 331–342.
[10] C. Li, S. Yu, H. Dong, C. Liu, H. Wu, H. Che, G. Chen, Appl. Catal. B: Environ. 238 (2018) 284–293.
[11] C. Li, S. Yu, Y. Wang, J. Han, H. Dong, G. Chen, J. Taiwan Inst. Chem. Eng. 87 (2018) 272–280.
[12] Y. Qu, X. Duan, Chem. Soc. Rev. 42 (2013) 2568–2580.
[13] H. Wang, L. Zhang, Z. Chen, J. Hu, S. Li, Z. Wang, J. Liu, X. Wang, Chem. Soc. Rev. 43 (2014) 5234–5244.

[14] Q. Xiang, J. Yu, M. Jaroniec, Chem. Soc. Rev. 41 (2012) 782–796.
[15] F. Wang, W.K.H. Ng, J.C. Yu, H. Zhu, C. Li, L. Zhang, Z. Liu, Q. Li, Appl. Catal. B: Environ. 111-112 (2012) 409–414.
[16] M. Zhu, S. Kim, L. Mao, M. Fujitsuka, J. Zhang, X. Wang, T. Majima, J. Am. Chem. Soc. 139 (2017) 13234–13242.
[17] X. Zhu, T. Zhang, Z. Sun, H. Chen, J. Guan, X. Chen, H. Ji, P. Du, S. Yang, Adv. Mater. 29 (2017) 1605776–1605782.
[18] G. Liu, L.-C. Yin, P. Niu, W. Jiao, H.-M. Cheng, Angew. Chem. Int. Ed. 52 (2013) 6242–6245.
[19] G. Liu, P. Niu, L. Yin, H.-M. Cheng, J. Am. Chem. Soc. 134 (2012) 9070–9073.
[20] L. Shi, P. Li, W. Zhou, T. Wang, K. Chang, H. Zhang, T. Kako, G. Liu, J. Ye, Nano Energy 28 (2016) 158–163.
[21] J. Liu, S. Wen, Y. Hou, F. Zuo, G.J.O. Beran, P. Feng, Angew. Chem. Int. Ed. 52 (2013) 3241–3245.
[22] X. Wang, K. Maeda, A. Thomas, K. Takanabe, G. Xin, J.M. Carlsson, K. Domen, M. Antonietti, Nat. Mater. 8 (2009) 76–80.
[23] K.I. Bolotin, K.J. Sikes, Z. Jiang, M. Klima, G. Fudenberg, J. Hone, P. Kim, H.L. Stormer, Solid State Commun. 146 (2008) 351–355.
[24] J.S. Bunch, A.M. van der Zande, S.S. Verbridge, I.W. Frank, D.M. Tanenbaum, J.M. Parpia, H.G. Craighead, P.L. McEuen, Science 315 (2007) 490–493.
[25] K.S. Novoselov, A.K. Geim, S.V. Morozov, D. Jiang, M.I. Katsnelson, I.V. Grigorieva, S.V. Dubonos, A.A. Firsov, Nature 438 (2005) 197–200.
[26] K.S. Novoselov, A.K. Geim, S.V. Morozov, D. Jiang, Y. Zhang, S.V. Dubonos, I.V. Grigorieva, A.A. Firsov, Science 306 (2004) 666–669.
[27] A. Pakdel, Y. Bando, D. Golberg, Chem. Soc. Rev. 43 (2014) 934–959.
[28] K. Watanabe, T. Taniguchi, H. Kanda, Nat. Mater. 3 (2004) 404–409.
[29] W. Lei, D. Portehault, D. Liu, S. Qin, Y. Chen, Nat. Commun. 4 (2013) 1777–1783.
[30] C. Zhi, Y. Bando, C. Tang, H. Kuwahara, D. Golberg, Adv. Mater. 21 (2009) 2889–2893.
[31] W. Lei, D. Portehault, R. Dimova, M. Antonietti, J. Am. Chem. Soc. 133 (2011) 7121–7127.
[32] D. Portehault, C. Giordano, C. Gervais, I. Senkovska, S. Kaskel, C. Sanchez, M. Antonietti, Adv. Funct. Mater. 20 (2010) 1827–1833.
[33] B. Rushton, R. Mokaya, J. Mater. Chem. 18 (2008) 235–241.
[34] C. Zhang, S. Zhao, C. Jin, A.L. Koh, Y. Zhou, W. Xu, Q. Li, Q. Xiong, H. Peng, Z. Liu, Nat. Commun. 6 (2015) 6519–6526.
[35] C. Zhao, Z. Xu, H. Wang, J. Wei, W. Wang, X. Bai, E. Wang, Adv. Funct. Mater. 24 (2014) 5985–5992.
[36] F. Guo, P. Yang, Z. Pan, X.-N. Cao, Z. Xie, X. Wang, Angew. Chem. 129 (2017) 8343–8347.
[37] L. Chen, X. Wang, Chem. Commun. 53 (2017) 11988–11991.
[38] C. Huang, C. Chen, M. Zhang, L. Lin, X. Ye, S. Lin, M. Antonietti, X. Wang, Nat. Commun. 6 (2015) 7698–7704.
[39] T. Ogi, Y. Kaihatsu, F. Iskandar, W.-N. Wang, K. Okuyama, Adv. Mater. 20 (2008) 3235–3238.
[40] M. Kawaguchi, T. Kawashima, T. Nakajima, Chem. Mater. 8 (1996) 1197–1201.
[41] L. Song, Z. Liu, A.L.M. Reddy, N.T. Narayanan, J. Taha-Tijerina, J. Peng, G. Gao, J. Lou, R. Vajtai, P.M. Ajayan, Adv. Mater. 24 (2012) 4878–4895.
[42] D.H. Kim, E. Byon, S. Lee, J.-K. Kim, H. Ruh, Thin Solid Films 447–448 (2004) 192–196.
[43] R.B. Kaner, J. Kouvetakis, C.E. Warble, M.L. Sattler, N. Bartlett, Mater. Res. Bull. 22 (1987) 399–404.

[44] K. Suenaga, C. Colliex, N. Demoncy, A. Loiseau, H. Pascard, F. Willaime, Science 278 (1997) 653–655.
[45] R.Y. Tay, H. Li, S.H. Tsang, M. Zhu, M. Loeblein, L. Jing, F.N. Leong, E.H.T. Teo, Chem. Mater. 28 (2016) 2180–2190.
[46] O. Baake, P.S. Hoffmann, A. Klein, B. Pollakowski, B. Beckhoff, W. Ensinger, M. Kosinova, N. Fainer, V.S. Sulyaeva, V. Trunova, X-Ray Spectrom. 38 (2009) 68–73.
[47] M.L. Kosinova, Y.M. Rumyantsev, N.I. Fainer, E.A. Maximovski, F.A. Kuznetsov, Nuclear instruments and methods in physics research section a: accelerators, spectrometers, Detect. Assoc. Equip. 470 (2001) 253–257.
[48] M.E. Bowden, I.W.M. Brown, G.J. Gainsford, H. Wong, Inorg. Chim. Acta 361 (2008) 2147–2153.
[49] A.W. Moore, S.L. Strong, G.L. Doll, M.S. Dresselhaus, I.L. Spain, C.W. Bowers, J.P. Issi, L. Piraux, J. Appl. Phys. 65 (1989) 5109–5118.
[50] Y.K. Yap, M. Yoshimura, Y. Mori, T. Sasaki, Appl. Phys. Lett. 80 (2002) 2559–2561.
[51] L. Ci, L. Song, C. Jin, D. Jariwala, D. Wu, Y. Li, A. Srivastava, Z.F. Wang, K. Storr, L. Balicas, F. Liu, P.M. Ajayan, Nat. Mater. 9 (2010) 430–435.
[52] Q. Weng, X. Wang, C. Zhi, Y. Bando, D. Golberg, ACS Nano 7 (2013) 1558–1565.
[53] Q. Weng, X. Wang, Y. Bando, D. Golberg, Adv. Energy Mater. 4 (2014) 1301525–1301532.
[54] M. Zhang, Z. Luo, M. Zhou, C. Huang, X. Wang, Sci. China-Mater. 58 (2015) 867–876.
[55] Y. Hong, C. Li, D. Li, Z. Fang, B. Luo, X. Yan, H. Shen, B. Mao, W. Shi, Nanoscale 9 (2017) 14103–14110.
[56] P. Niu, L. Zhang, G. Liu, H.-M. Cheng, Adv. Funct. Mater. 22 (2012) 4763–4770.
[57] Y. Gong, G. Shi, Z. Zhang, W. Zhou, J. Jung, W. Gao, L. Ma, Y. Yang, S. Yang, G. You, R. Vajtai, Q. Xu, A.H. MacDonald, B.I. Yakobson, J. Lou, Z. Liu, P.M. Ajayan, Nat. Commun. 5 (2014) 3193–3200.
[58] L. Ge, F. Zuo, J. Liu, Q. Ma, C. Wang, D. Sun, L. Bartels, P. Feng, J. Phys. Chem. C 116 (2012) 13708–13714.
[59] S.Y. Kim, J. Park, H.C. Choi, J.P. Ahn, J.Q. Hou, H.S. Kang, J. Am. Chem. Soc. 129 (2007) 1705–1716.
[60] Q. Liang, Z. Li, X. Yu, Z.-H. Huang, F. Kang, Q.-H. Yang, Adv. Mater. 27 (2015) 4634–4639.
[61] M. Zhang, X. Wang, Energy Environ. Sci. 7 (2014) 1902–1906.
[62] X. Lu, K. Xu, P. Chen, K. Jia, S. Liu, C. Wu, J. Mater. Chem. A 2 (2014) 18924–18928.
[63] S. Yang, Y. Gong, J. Zhang, L. Zhan, L. Ma, Z. Fang, R. Vajtai, X. Wang, P.M. Ajayan, Adv. Mater. 25 (2013) 2452–2456.
[64] J. Zhang, X. Chen, K. Takanabe, K. Maeda, K. Domen, J.D. Epping, X. Fu, M. Antonietti, X. Wang, Angew. Chem., Int. Ed. 49 (2010) 441–444.
[65] Q. Han, B. Wang, J. Gao, Z. Cheng, Y. Zhao, Z. Zhang, L. Qu, ACS Nano 10 (2016) 2745–2751.
[66] Q. Han, B. Wang, Y. Zhao, C. Hu, L. Qu, Angew. Chem., Int. Ed. 54 (2015) 11433–11437.
[67] Q. Liang, Z. Li, Z.-H. Huang, F. Kang, Q.-H. Yang, Adv. Funct. Mater. 25 (2015) 6885–6892.
[68] G. Liu, P. Niu, C. Sun, S.C. Smith, Z. Chen, G.Q. Lu, H.-M. Cheng, J. Am. Chem. Soc. 132 (2010) 11642–11648.
[69] G. Zhang, M. Zhang, X. Ye, X. Qiu, S. Lin, X. Wang, Adv. Mater. 26 (2014) 805–809.
[70] J. Zhang, G. Zhang, X. Chen, S. Lin, L. Möhlmann, G. Dołęga, G. Lipner, M. Antonietti, S. Blechert, X. Wang, Angew. Chem. 124 (2012) 3237–3241.